J Mater Sci: Mater Electron (2026) 37:150

Hierarchical ZnO-NR@C/Al_2O_3-NF composite: a durable binder-free electrode for advanced supercapacitors

Ali B. M. Ali[1], Asilbek Abdullaev[2], Elyor Saitov[3], M. Sudhakara Reddy[4], Badri Narayan Sahu[5], Sridharan Sundharam[6], Sanjeev Kumar[7], Mustafa Diab[8,*], H. Amin El Sabban[9,*], Aseel Smerat[10], and Mumtaj Shah[11]

[1] *Advanced Technical College, University of Warith Al-Anbiyaa, Karbala, Iraq*
[2] *Kimyo International University in Tashkent, Shota Rustaveli Str. 156, 100121 Tashkent, Uzbekistan*
[3] *University of Tashkent for Applied Sciences, Str. Gavhar 1, 100149 Tashkent, Uzbekistan*
[4] *Department of Physics & Electronics, School of Sciences, JAIN (Deemed to Be University), Bangalore, Karnataka, India*
[5] *Department of Electronics & Communication Engineering, Siksha O Anusandhan (Deemed to Be University), Bhubaneswar, Odisha 751030, India*
[6] *Department of Physics, Sathyabama Institute of Science and Technology, Chennai, Tamil Nadu, India*
[7] *Department of Physics, University Institute of Sciences, Chandigarh University, Mohali, Punjab, India*
[8] *Medical Laboratory Technique College, The Islamic University, Najaf, Iraq*
[9] *College of Dentistry, Alnoor University, Mosul, Iraq*
[10] *Hourani Center for Applied Scientific Research, Al-Ahliyya Amman University, Amman 19328, Jordan*
[11] *Department of Chemical Engineering, College of Engineering, King Khalid University Abha, 61141 Abha, Saudi Arabia*

Received: 25 August 2025
Accepted: 24 December 2025

ABSTRACT

Developing advanced supercapacitor electrodes with both high energy density and long-term cycling stability is a critical challenge in energy storage. While metal oxides like zinc oxide (ZnO) offer high theoretical pseudocapacitance, they often suffer from poor electrical conductivity and structural degradation during cycling. To overcome these limitations, we designed and fabricated a novel, binder-free hierarchical composite, carbon-coated zinc oxide Nanorod@ Aluminum Oxide Nanofiber (ZnO–NR@C/Al_2O_3–NF), where a stable alumina nanofiber scaffold and a conductive carbon coating work synergistically to enhance the performance of ZnO nanorods. The composite was synthesized via a multi-step approach. First, a robust Al_2O_3–NF scaffold was fabricated by electrospinning followed by high-temperature calcination. Next, ZnO–NR were grown directly onto the scaffold using a hydrothermal method. Finally, a uniform, porous carbon layer was coated onto the ZnO nanorods through hydrothermal carbonization of glucose and subsequent annealing. Comprehensive characterization confirmed the successful synthesis of a unique, hierarchical, and highly porous architecture. Further analyses using XRD and XPS verified the composite's

Address correspondence to E-mail: diabmustafa.rh9034@gmail.com; hebaaelsabban61@gmail.com

https://doi.org/10.1007/s10854-025-16516-x
Published online: 08 January 2026

high purity, expected crystallographic phases, and crucial electronic interactions between the carbon coating and the metal oxides. Most significantly, the electrode demonstrates outstanding long-term durability, maintaining its structural and crystallographic integrity with minimal degradation after 8000 charge–discharge cycles. This exceptional stability is attributed to the synergistic design, where the Al_2O_3 scaffold provides mechanical support and the carbon coating enhances conductivity while preventing the pulverization of the active ZnO material, validating its potential for high-performance energy storage applications.

1 Introduction

The escalating global energy demand and the urgent need to transition toward renewable energy sources have critically highlighted the importance of advanced electrochemical energy storage (EES) systems [1–3]. These systems are pivotal for bridging the gap between intermittent energy generation and consistent power supply. Among various EES technologies, supercapacitors (SCs), also known as ultracapacitors, have emerged as highly promising devices. They distinguish themselves with an exceptionally high power density, enabling rapid charge and discharge capabilities far exceeding those of conventional batteries [4–6]. Furthermore, their remarkable longevity, often enduring hundreds of thousands of cycles with minimal degradation, and their wide operational temperature range make them ideal for applications requiring quick energy bursts and robust performance, such as in electric vehicles, consumer electronics, and grid stabilization [7–9].

Despite their advantages, the widespread application of SCs is often hampered by their relatively low energy density, which limits the amount of energy they can store per unit mass or volume [10–12]. To overcome this, current research is intensely focused on developing advanced electrode materials. While carbon-based materials excel in electric double-layer capacitance (EDLC), their energy storage is fundamentally limited [13–15]. Porous metal oxides, on the other hand, offer the potential for much higher energy density through fast surface redox reactions, a mechanism known as pseudocapacitance. However, they typically suffer from poor electrical conductivity and significant volume changes during cycling, leading to poor rate capability and instability [16–19]. A promising strategy to mitigate these issues is the development of nanocomposites, where metal oxides are supported on or coated with a conductive carbon layer, creating a synergistic material with enhanced conductivity, structural stability, and electrochemical performance.

Recent literature provides compelling evidence for the success of designing composite electrodes to overcome the individual limitations of metal oxides. For instance, Sanni et al. [20] demonstrated that doping ZnO with a small amount of γ-Al_2O_3 transformed ZnO nanoflakes into elongated nanorods, which, when combined with a redox-active electrolyte, achieved a specific capacity of 267 C/g and excellent stability over 9000 cycles. Similarly, Asangi et al. [21] fabricated a binary nanocomposite of Al_2O_3 and CuO, revealing a remarkable synergistic effect that resulted in a high specific capacitance of 864 F/g and a capacitance retention of 85% after 5000 cycles, far exceeding the performance of the individual oxides. Further showcasing the benefits of multi-component systems, Gao et al. [22] engineered free-standing ZnO/carbon nanofiber electrodes and augmented them with multivalent vanadium. This approach yielded a high areal capacitance of 780.5 mF/cm^2 and 97% capacitance retention after 10,000 cycles, highlighting the advantages of integrating transition metals with ZIF-derived ZnO in a conductive carbon matrix. These studies collectively underscore a clear trend: creating hierarchical, multi-component nanostructures is a highly effective strategy for boosting the electrochemical performance and durability of SC electrodes.

This work introduces a novel three-dimensional, binder-free electrode material by strategically integrating zinc oxide (ZnO), aluminum oxide (Al_2O_3), and a porous carbon coating. ZnO is an attractive pseudocapacitive material due to its high theoretical capacitance, low cost, and environmental benignity [23–25]. Al_2O_3, while not electrochemically active, is exceptionally stable chemically and thermally, making it an ideal candidate for a robust, high-surface-area structural scaffold [26–29]. The final component, a porous carbon coating, is crucial as it encases the active material, creating a highly conductive pathway

for rapid electron transport and acting as a flexible buffer to accommodate any strain during ion intercalation. The proposed Carbon-coated Zinc Oxide Nanorod@Aluminum Oxide Nanofiber (ZnO-NR@C/Al_2O_3-NF) architecture is designed to harness a powerful synergistic effect: the Al_2O_3 nanofibers provide a stable backbone, the ZnO nanorods grown upon it offer high charge storage capacity, and the conformal carbon layer electrically wires the system together while ensuring mechanical stability. This unique hierarchical design is expected to yield superior SC performance with high specific capacitance, excellent rate capability, and outstanding long-term cycling stability.

To address the critical challenge of balancing energy density and long-term stability in supercapacitors, this study presents the rational design and synthesis of a novel, binder-free ZnO–NR@C/Al_2O_3–NF hierarchical composite. The primary contribution of this work is the creation of a multi-component architecture where each component serves a specific, synergistic function to overcome the individual limitations of metal oxides. The fabrication process involves a facile, multi-step approach beginning with the electrospinning of a free-standing Al_2O_3 nanofiber (Al_2O_3–NF) mat, which acts as a robust mechanical scaffold. High-density, pseudocapacitive ZnO nanorods (ZnO–NR) are then grown directly onto this scaffold via a hydrothermal method. Finally, a uniform, porous carbon coating is applied through hydrothermal carbonization and subsequent annealing to ensure high electrical conductivity and buffer the active material against mechanical stress. Through a suite of systematic physicochemical characterization techniques, including FESEM, XRD, and XPS analysis, we thoroughly investigate the unique morphology, crystal structure, and surface chemistry of the composite. This detailed investigation, coupled with a comprehensive electrochemical evaluation, validates our design strategy and establishes the ZnO–NR@C/Al_2O_3–NF composite as a highly promising and durable electrode for next-generation SCs.

2 Experimental section

2.1 Materials

Aluminum nitrate nonahydrate ($Al(NO_3)_3{\cdot}9H_2O$), polyvinylpyrrolidone (PVP, Mw = 360,000 g/mol), N,N–dimethylformamide (DMF), ethanol (C_2H_5OH), zinc nitrate hexahydrate ($Zn(NO_3)_2{\cdot}6H_2O$), hexamethylenetetramine (HMTA, $C_6H_{12}N_4$), D-(+)-glucose ($C_6H_{12}O_6$), hydrochloric acid (HCl), and potassium hydroxide (KOH) were purchased from Sigma-Aldrich and used as received without further purification. Deionized (DI) water was used in all experiments.

2.2 Synthesis of alumina nanofiber (Al_2O_3-NF) scaffold

The alumina nanofiber scaffold was fabricated via an electrospinning technique followed by calcination. First, a precursor solution was prepared by dissolving 1.5 g of $Al(NO_3)_3{\cdot}9H_2O$ and 1.0 g of PVP in a solvent mixture of 5 mL of DMF and 5 mL of ethanol. The solution was stirred vigorously for 12 h at room temperature to ensure homogeneity.

The resulting viscous solution was loaded into a 10 mL plastic syringe fitted with a 22-gauge stainless steel needle. Electrospinning was performed at an applied voltage of 20 kV, with a tip-to-collector distance of 15 cm and a constant feed rate of 0.5 mL/h. The as-spun nanofibers were collected on a piece of aluminum foil. Finally, the collected mat of as-spun nanofibers was carefully peeled from the foil and calcined in a muffle furnace at 800 °C for 3 h in an air atmosphere with a heating rate of 5 °C/min to remove the PVP and convert the aluminum nitrate to crystalline Al_2O_3.

2.3 Growth of ZnO nanorods on Al_2O_3-NF scaffold (ZnO-NR/Al_2O_3-NF)

ZnO nanorods were grown on the surface of the calcined Al_2O_3-NF scaffold using a hydrothermal method. In a typical synthesis, an aqueous growth solution was prepared by dissolving 0.025 M zinc nitrate hexahydrate and 0.025 M hexamethylenetetramine in 100 mL of DI water. The solution was stirred for 30 min.

The previously prepared Al_2O_3-NF scaffold (a piece of approximately 2 cm × 4 cm) was immersed into the growth solution in a Teflon-lined stainless steel autoclave. The autoclave was sealed and maintained at 95 °C for 6 h. After the reaction, the autoclave was allowed to cool down to room temperature naturally. The resulting ZnO-NR/Al_2O_3-NF composite was removed from the solution, rinsed

thoroughly with DI water and ethanol to remove any residual salts, and dried in an oven at 60 °C for 12 h.

2.4 Carbon Coating of ZnO-NR/Al_2O_3-NF (ZnO-NR@C/Al_2O_3-NF)

A porous carbon layer was coated onto the ZnO nanorods via hydrothermal carbonization of glucose. The dried ZnO-NR/Al_2O_3-NF composite was placed in a Teflon-lined autoclave containing a 0.5 M aqueous solution of D–(+)-glucose. The autoclave was heated to 180 °C and held for 8 h. After cooling, the composite turned a brownish color, indicating the formation of a glucose-derived polymer layer.

The composite was then washed with DI water and ethanol and dried. To convert the polymer layer into amorphous carbon, the sample was annealed at 500 °C for 2 h under an argon (Ar) atmosphere with a heating rate of 5 °C/min. The final product was a black, free-standing mat of the ZnO-NR@C/Al_2O_3-NF composite.

2.5 Material characterization

The morphology and microstructure of the synthesized materials were examined using Field Emission Scanning Electron Microscopy (FESEM, Zeiss SEM) equipped with an Energy-Dispersive X-ray Spectroscopy (EDS) detector for elemental analysis. The crystal structure and phase purity of the composites were determined by X-ray Diffraction (XRD) on a Bruker D8 Advance diffractometer with Cu Kα radiation ($\lambda = 1.5406$ Å). X-ray photoelectron spectroscopy (XPS) conducted on a Thermo Scientific K-Alpha instrument provided insights into the surface chemical states and elemental valences of the samples.

2.6 Electrochemical measurements

Electrochemical investigations were carried out on the assembled SCs using a Galvanostat/Potentiostat system (Vertex One, Ivium Technologies, Netherlands) in a two-electrode configuration. The devices were constructed from ZnO-NR/Al_2O_3-NF and ZnO-NR@C/Al_2O_3-NF electrodes, with a filter paper soaked in 6 M KOH functioning as the ion-conducting separator. The electrochemical response of the SCs was examined through cyclic voltammetry (CV), galvanostatic charge–discharge (GCD), and electrochemical impedance spectroscopy (EIS). For the EIS experiments, an AC perturbation of 5 mV was applied at the open-circuit potential to evaluate resistance and capacitive behavior.

3 Results and discussion

3.1 Characterization results

The step-by-step morphological evolution of the composite electrode was investigated using Field Emission Scanning Electron Microscopy (FESEM). Figure 1a visually confirms the material's large-scale morphology as a white, free-standing, paper-like scaffold, while Fig. 1a, b reveal the microstructure of the initial Al_2O_3–NF scaffold after calcination. The images show a highly porous, three-dimensional network composed of interconnected, smooth-surfaced alumina nanofibers. This structure serves as a robust backbone for the electrode, providing mechanical integrity and a high surface area that acts as an excellent platform for the subsequent uniform deposition of the active material. While chemically stable, the electrically insulating nature of this alumina scaffold necessitates the addition of conductive phases in later steps.

Following the hydrothermal growth process, the morphology of the composite changes dramatically, as seen in the FESEM images of the ZnO–NR/Al_2O_3–NF sample in Fig. 1c, d. The original alumina nanofibers are now completely and uniformly covered by a dense array of ZnO nanorods. These nanorods grow vertically outwards from the scaffold, creating a hierarchical structure with a significantly increased surface area. This specific nanorod morphology is highly advantageous for SC performance; it provides a high density of electrochemically active sites for charge storage and creates direct, unobstructed pathways for efficient electrolyte ion diffusion, ensuring rapid charge–discharge kinetics.

The final morphology of the ZnO-NR@C/Al_2O_3-NF catalyst is presented in Fig. 1e, g. After carbon coating, the well-defined nanorod array structure is perfectly preserved. However, the surface of the nanorods now appears rougher and slightly thicker, indicating the successful deposition of a porous carbon layer. This final modification is critical and serves multiple functions to boost

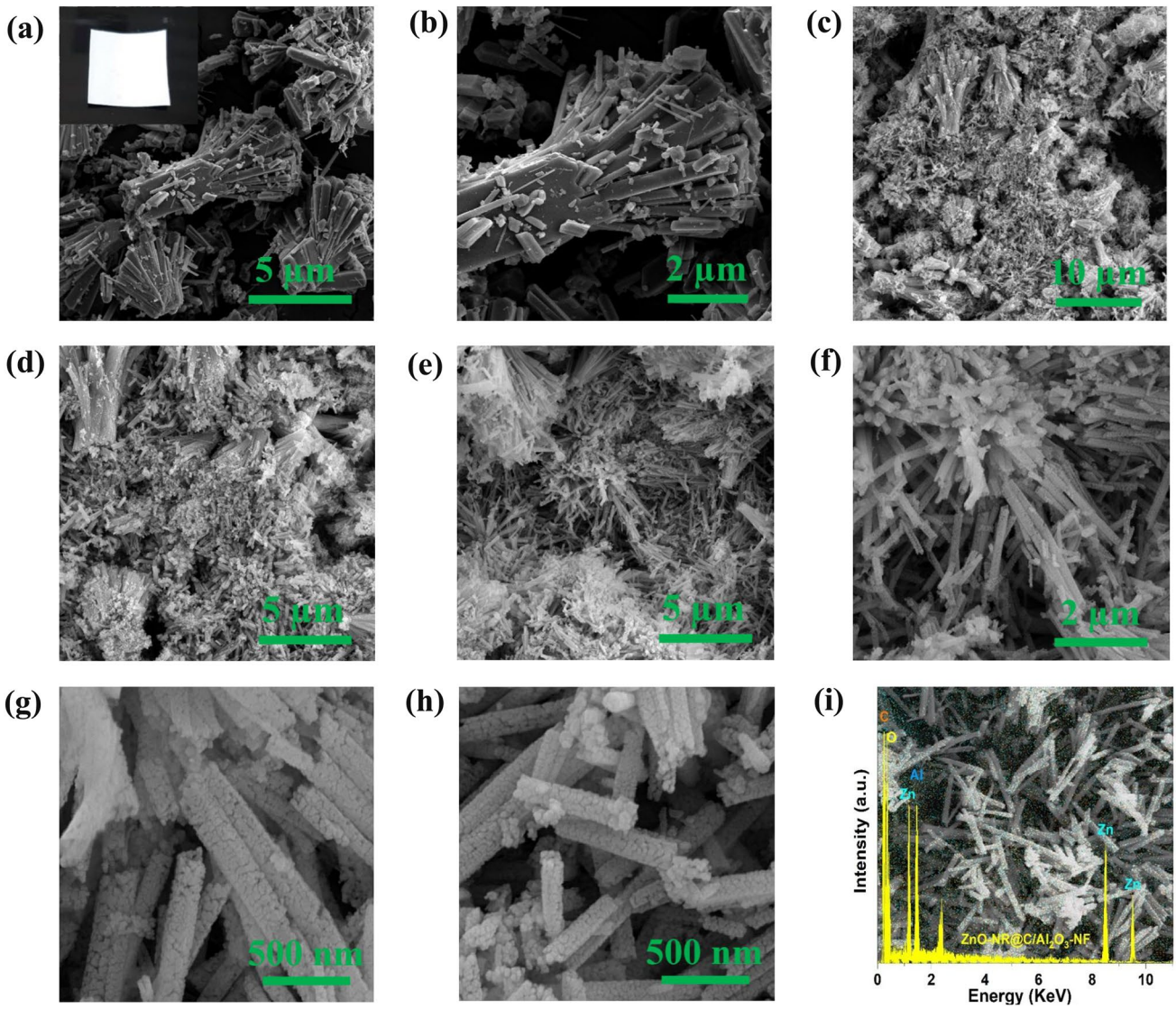

Fig. 1 FESEM images of Al_2O_3-NF (**a**-**b**), (inside: photograph of Al_2O_3-NF scaffold), ZnO-NR/Al_2O_3-NF composite (**c**-**d**), ZnO-NR@C/Al_2O_3-NF composite (**e**–**g**), FESEM of ZnO-NR@C/Al_2O_3-NF sample after stability test (**h**), EDS spectrum and EDS elemental mapping images of prepared ZnO-NR@C/Al_2O_3-NF composite (**i**)

electrochemical performance. Firstly, the carbon coating creates a continuous conductive network throughout the electrode, effectively overcoming the poor conductivity of both the ZnO semiconductor and the underlying Al_2O_3 insulator. Secondly, it acts as a protective shell, physically binding the ZnO nanorods to the scaffold and preventing their agglomeration or detachment during strenuous charge–discharge cycles, which greatly enhances long-term stability. Finally, the inherent porosity of the carbon layer itself introduces additional channels for electrolyte transport, maximizing the accessible surface area and ensuring that ions can efficiently reach the entire ZnO core for Faradaic reactions. The long-term operational stability of the ZnO–NR@C/Al_2O_3–NF electrode, a critical parameter for practical applications, was evaluated through extended galvanostatic charge–discharge cycling. To assess its structural resilience, the electrode's morphology was examined after being subjected to 5000 consecutive cycles. Remarkably, as shown in the post-cycling analysis in Fig. 1h, the hierarchical nanorod architecture remains exceptionally well-preserved. The integrity of the nanorods is maintained without any

signs of significant pulverization, detachment, or structural collapse. This outstanding durability is a direct result of the composite's intelligent, multi-component design. The robust Al_2O_3 nanofiber scaffold provides a stable mechanical backbone, while the conformal carbon coating acts as a crucial protective shell. This carbon layer effectively absorbs the mechanical stress induced by repeated ion insertion/extraction, preventing the degradation of the active ZnO material. This synergistic interplay between the stable scaffold and the protective coating ensures the electrode's structural integrity, validating its potential for highly stable and dependable long-term electrochemical energy storage.

Energy-dispersive X-ray spectroscopy (EDS) was conducted to verify the elemental composition and spatial distribution within the final ZnO-NR@C/Al_2O_3-NF composite. The resulting EDS spectrum, presented in Fig. 1h, unambiguously confirms the presence of all expected elements. Distinct peaks corresponding to Zinc (Zn), Aluminum (Al), Oxygen (O), and Carbon (C) dominate the spectrum, validating the successful synthesis and accurate formation of the multi-component material. The detection of Zn, Al, and O corroborates the retention of the respective metal oxide phases, while the prominent C signal originates from the crucial conductive coating. Notably, the absence of any extraneous elemental peaks underscores the high purity of the composite, which is essential for minimizing parasitic side reactions and ensuring stable electrochemical performance.

Even more critical than composition is the elemental distribution, which was visualized through EDS mapping, as shown in Fig. 1i. The maps reveal a remarkable spatial correlation between the constituent elements across the nanostructured morphology. This uniform distribution is a critical factor for ensuring consistent electrochemical activity across the entire porous nanorod surface. It ensures that every electrochemically active site on the vast surface area of the nanorods has an efficient, direct pathway for electron transport.

The crystallographic structure and phase composition of the final ZnO-NR@C/Al_2O_3-NF composite were investigated using X-ray diffraction (XRD), with the resulting pattern displayed in Fig. 2a. The analysis provides definitive evidence for the successful synthesis of the multi-component material, revealing a combination of sharp, crystalline peaks and a broad amorphous signature.

The diffractogram exhibits a series of well-defined, intense peaks that can be precisely indexed to two distinct crystalline phases. The peaks at 2θ values of 31.7°, 34.4°, and 36.2° correspond to the (100), (002), and (101) planes of the hexagonal wurtzite ZnO phase, respectively, which is in excellent agreement with JCPDS card No. 36–1451 [30, 31]. Concurrently, another set of diffraction peaks, including those at 25.6°, 35.1°, and 43.4°, are clearly attributable to the (012), (104), and (113) planes of α-Al_2O_3 (corundum), matching JCPDS card No. 10–0173 [32, 33]. The sharpness of these peaks indicates the high crystallinity of both the ZnO nanorods and the alumina nanofiber scaffold.

Underlying these sharp crystalline peaks, a broad, low-intensity hump is discernible in the 2θ range of 20–30°. This feature is the characteristic signature of amorphous carbon, confirming the presence of the non-crystalline carbon coating [34]. The superposition of all three distinct signatures, wurtzite ZnO, corundum Al_2O_3, and amorphous carbon, in a single pattern validates the successful fabrication of the ZnO-NR@C/Al_2O_3-NF hierarchical composite and confirms the integrity of each component after the multi-step synthesis. To further investigate the material's structural integrity, X-ray diffraction (XRD) analysis was performed on the ZnO-NR@C/Al_2O_3-NF electrode after the extended 5,000-cycle durability test. The post-cycling XRD pattern, presented in Fig. 2b, is nearly identical to that of the pristine, uncycled electrode. The characteristic diffraction peaks for both the wurtzite ZnO and α–Al_2O_3 phases are fully retained with no significant changes in intensity or position. Crucially, the absence of any new or extraneous peaks confirms that the material did not undergo any phase transformation or chemical degradation during the prolonged electrochemical cycling. This remarkable crystallographic stability demonstrates the electrochemical robustness of the composite. It indicates that the amorphous carbon coating effectively shields the crystalline ZnO nanorods, preserving their structure under strenuous operational conditions. This enduring structural integrity is fundamental to the material's excellent long-term performance, validating its design as a durable and reliable electrode for advanced SCs.

X-ray photoelectron spectroscopy (XPS) was utilized to analyze the surface elemental composition and chemical bonding states of the synthesized materials. The deconvoluted XPS spectra (Fig. 2c–f) for the individual elements in both the ZnO-NR/Al_2O_3-NF and

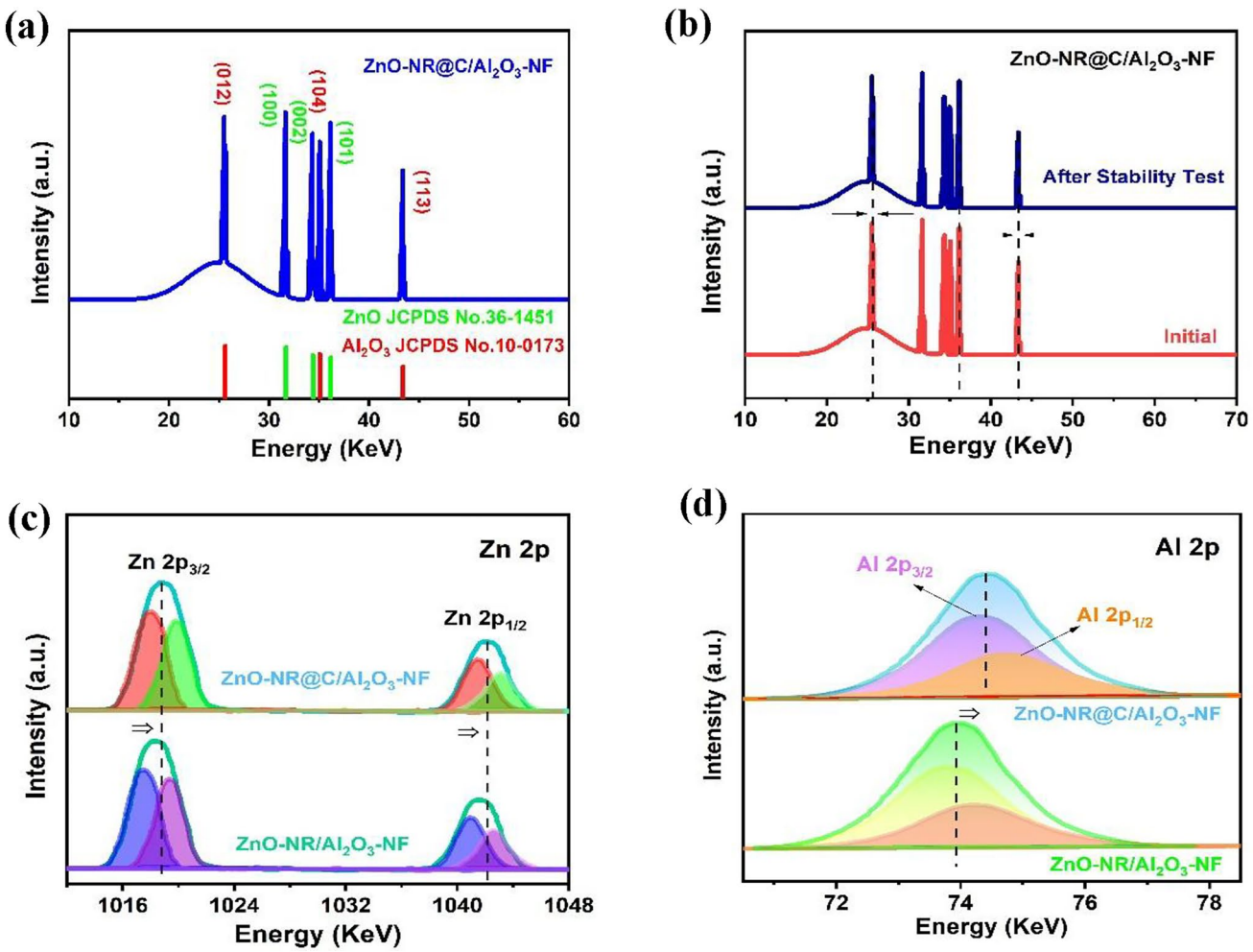

Fig. 2 XRD patterns of synthesized ZnO-NR@C/Al_2O_3-NF composite before (**a**), and After stability measurement (**b**). The high-resolution XPS spectra of prepared composites **c** Zn 2p; **d** Al 2p, **e** O 1 s, and **f** C 1 s. **g** N_2 adsorption/desorption isotherms and **h** PSDs of Al_2O_3-NF, ZnO-NR/Al_2O_3-NF, and ZnO-NR@C/Al_2O_3-NF composite

the final ZnO-NR@C/Al_2O_3-NF composites clearly confirm the presence of zinc (Zn), aluminum (Al), oxygen (O), and carbon (C). These results provide definitive evidence for the successful synthesis of the ZnO-NR@C/Al_2O_3-NF composite. Moreover, the absence of any extraneous peaks or contamination within the instrument's detection limits attests to the high purity of the fabricated materials. The deconvoluted Zn 2p spectra for both ZnO-NR/Al_2O_3-NF and ZnO-NR@C/Al_2O_3-NF, presented in Fig. 2c, display well-defined peaks appearing around 1018.1 and 1019.2 eV for Zn $2p_{3/2}$, and 1042.2 and 1043.2 eV for Zn $2p_{1/2}$. These peak positions confirm that zinc predominantly exists in the + 2 oxidation state within the samples [35]. The chemical state of aluminum within the nanofiber scaffold was investigated via the high-resolution Al 2p XPS spectrum, presented in Fig. 2d. For the final ZnO–NR@C/Al_2O_3–NF composite, the spectrum is dominated by a strong peak centered at a binding energy of approximately 74.7 eV. This position is the characteristic signature of aluminum in the Al^{3+} oxidation state, bonded to oxygen within an aluminum oxide (Al_2O_3) lattice. This finding confirms that the chemical integrity of the alumina scaffold was successfully preserved throughout the multi-step synthesis. A deconvolution of this peak may reveal a primary component related to the Al-O bonds of the corundum lattice and a smaller, lower-energy shoulder (around 74.2 eV) which can be attributed to surface aluminol (Al–OH) groups. The analysis confirms that aluminum exists exclusively in its oxidized state, which is crucial

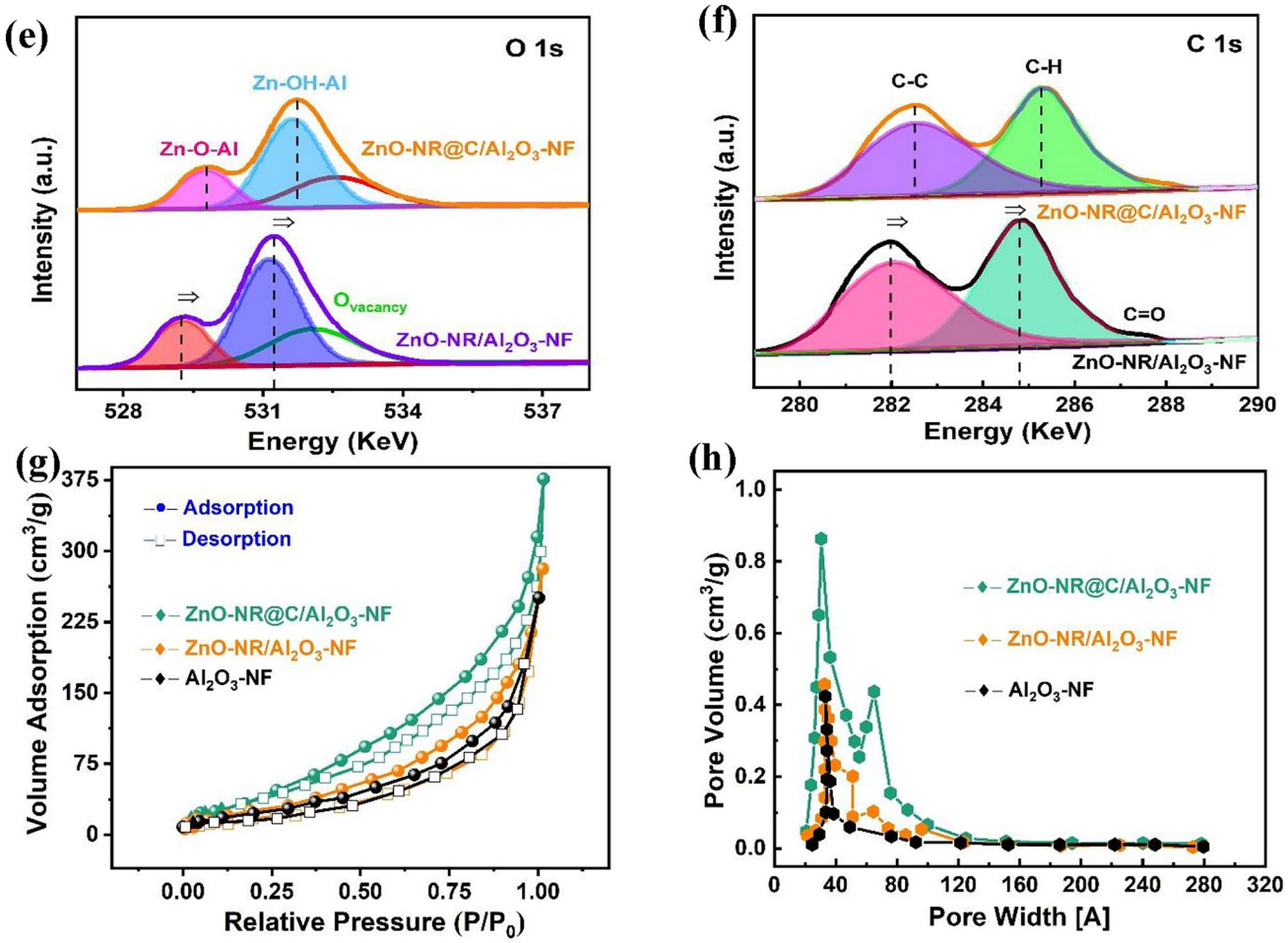

Fig. 2 continued

for the chemical stability of the electrode's backbone [36].

The chemical environment of oxygen within the composites was examined by deconvoluting the high-resolution O 1s spectrum, as shown in Fig. 2e. The spectrum can be resolved into three distinct components, revealing different types of oxygen bonding on the material's surface. The dominant peak, located at the lowest binding energy of approximately 529.3 eV, is assigned to lattice oxygen. This component represents oxygen atoms fully bonded within the metal oxide crystal structures of both ZnO and Al_2O_3 (M–O–M). The second peak, centered around 531.1 eV, is attributed to oxygen in hydroxyl groups (M–OH). These species are typically found on the surface of metal oxides and are known to be electrochemically active sites that contribute to pseudocapacitance. The third component, at the highest binding energy of about 532.2 eV, corresponds to loosely bound or physisorbed water molecules (H–O–H) on the material's surface [37]. This detailed analysis of the O 1s spectrum confirms the integrity of the metal oxide framework and identifies the presence of surface functional groups that are crucial for the electrode–electrolyte interaction. The high-resolution C 1s XPS spectrum (Fig. 2f) provides definitive evidence of the successful carbon coating on the final ZnO–NR@C/Al_2O_3–NF composite. The complex C 1s envelope can be deconvoluted into three primary peaks, indicating a variety of carbon bonding environments. The most intense peak, centered at a binding energy of approximately 284.8 eV, is assigned to the sp^2-hybridized C = C bonds that form the graphitic-like framework of the amorphous carbon layer. This conductive carbon skeleton is fundamental to improving the overall electrical conductivity of the composite electrode. A second peak at a higher binding energy, around 287.7 eV, is attributed

to oxygenated carbon species. This component represents carbon atoms bonded to oxygen, likely in the form of hydroxyl (C–O) and carbonyl (C = O) functional groups on the surface. A smaller peak, often observed around 286.1 eV (not explicitly mentioned but common), corresponds to sp^3-hybridized C–C bonds or C–O single bonds, representing defects or different functional groups within the carbon structure. The presence of the conductive sp^2 carbon network ensures rapid electron transport, while the oxygen-containing functional groups enhance the surface wettability, improving the interfacial contact with the aqueous electrolyte and facilitating more efficient charge transfer [38, 39]. A comparison of the high-resolution spectra for the ZnO-NR/Al_2O_3-NF and ZnO-NR@C/Al_2O_3-NF samples reveals subtle but significant shifts in the binding energies of the core elements (Fig. 2c–f). These shifts are indicative of a strong electronic interaction at the interface between the carbon coating and the underlying metal oxide nanorods. This interaction signifies a redistribution of electron density at the material's surface, which is crucial for enhancing electrochemical performance. By creating a tightly coupled interface, the carbon layer facilitates more efficient electron mobility and expedites charge transfer kinetics to and from the active Al_2O_3 and ZnO sites. This synergistic effect is a key factor contributing to the superior SC efficiency of the final composite. In summary, the comprehensive XPS analysis confirms not only the successful fabrication and high purity of the ZnO-NR@C/Al_2O_3-NF composite but also reveals the fundamental electronic coupling between its components. This intimate interfacial connection is directly responsible for boosting charge transfer efficiency and electrochemical activity, providing a clear rationale for its outstanding performance as a SC electrode.

The textural properties and porous nature of the synthesized materials were systematically investigated using Nitrogen (N_2) adsorption–desorption analysis, with the isotherms presented in Fig. 2g and the pore size distributions (PSDs) in Fig. 2h.

All three samples exhibit a characteristic Type IV isotherm with a distinct Type H3 hysteresis loop in the high relative pressure range ($P/P_0 > 0.7$), confirming the presence of mesoporous structures within the interconnected nanofiber and nanorod aggregates.

The calculated BET specific surface area (S_{BET}) and total pore volume (V_t) confirm a progressive increase in porosity with each synthetic step: The initial Al_2O_3-NF scaffold showed a surface area of 21 $m^2 \cdot g^{-1}$ and a total pore volume of 0.032 $cm^3 \cdot g^{-1}$. After the growth of ZnO nanorods, the ZnO-NR/Al_2O_3-NF intermediate showed an increase, reaching 26 $m^2 \cdot g^{-1}$ and 0.038 $cm^3 \cdot g^{-1}$, indicating that the nanorods created additional surface area without blocking the existing channels. The final ZnO–NR@C/Al_2O_3–NF composite exhibited the most significant enhancement, achieving a S_{BET} of 43 $m^2 \cdot g^{-1}$ and a V_t of 0.059 $cm^3 \cdot g^{-1}$. This final composition boasts a surface area approximately 1.8 times greater and a pore volume over twice that of the pristine Al_2O_3-NF scaffold, directly validating the success of the multi-step hierarchical synthesis. The Pore Size Distribution (PSD) of the final ZnO-NR@C/Al_2O_3-NF composite exhibits a complex multimodal structure, which strongly supports the material's higher quantitative values. This hierarchical porosity is characterized by three distinct features: a sharp, new peak around 30 Å, which is attributed to the micropores and small mesopores inherent to the porous carbon layer and crucial for facilitating fast ion transport kinetics; an intensified mesopore peak around 38 Å, confirming the preservation and utilization of the channels within the underlying scaffold structure; and a third, broader distribution of larger mesopores centered around 70–75 Å, which represents the newly created voids and macroporous channels formed between the assembled carbon-coated nanorods, acting as electrolyte reservoirs. This structure is critical for supercapacitor performance, as it maximizes the available electrochemical active sites and ensures highly efficient pathways for rapid electrolyte ion diffusion.

3.2 Electrochemical Performance

The electrochemical performance of ZnO-NR/Al_2O_3–NF and ZnO-NR@C/Al_2O_3–NF electrodes was evaluated in a symmetric two-electrode configuration using 6 M KOH electrolyte. Cyclic voltammetry carried out in the potential range of 0–0.9 V at scan rates between 10 and 100 mV s^{-1} (Figs. 3a, b) revealed distinct Faradaic features in both electrodes, confirming the pseudocapacitive character of the charge storage process. Compared with the uncoated ZnO–NR/Al_2O_3–NF, the carbon-modified ZnO–NR@C/Al_2O_3–NF exhibited significantly enlarged CV profiles and more intense redox currents, which clearly demonstrate the superior utilization of active sites and enhanced electrochemical activity. This

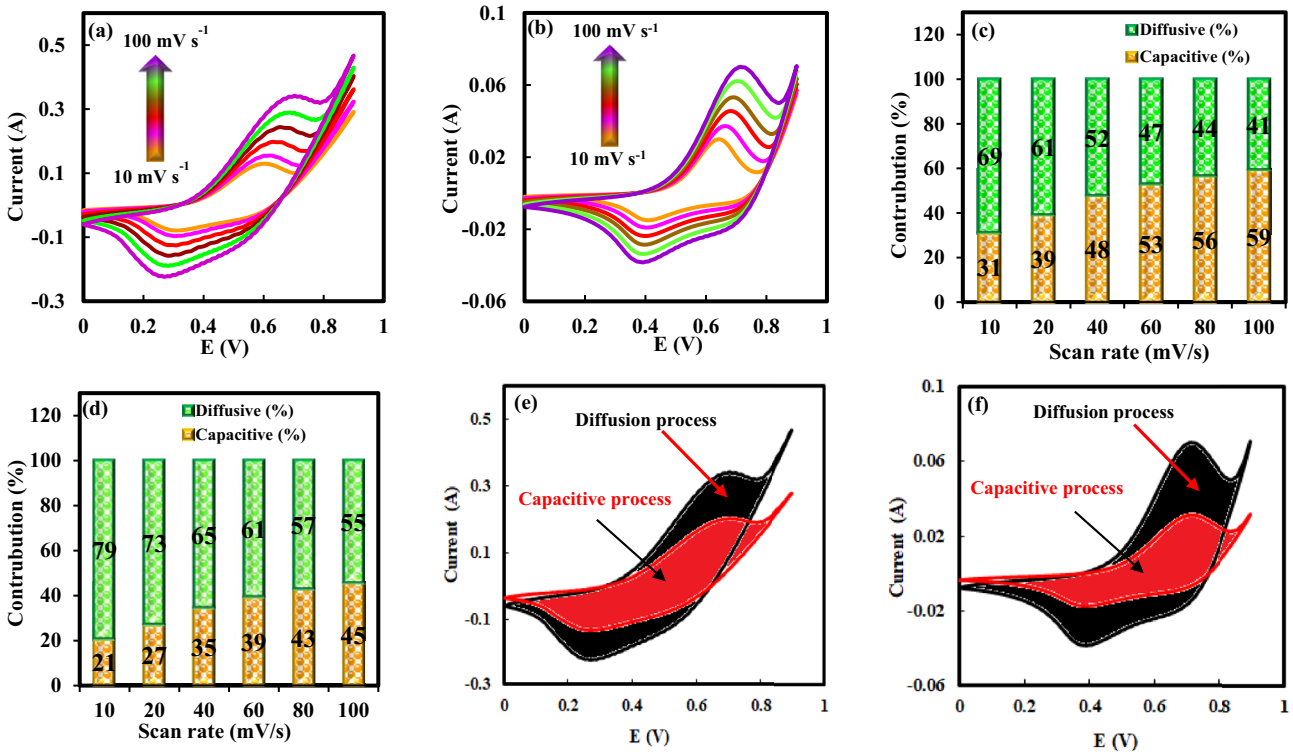

Fig. 3 Cyclic voltammetry curves of SCs based on **a** ZnO-NR@C/Al_2O_3–NF and **b** ZnO-NR/Al_2O_3–NF electrodes recorded at different scan rates. **c**, **d** Kinetic separation of capacitive and diffusion-controlled contributions at various scan rates for both systems. **e**, **f** Comparative evaluation of surface-controlled charge storage fractions, emphasizing the enhanced capacitive dominance and superior redox activity of the ZnO-NR@C/Al_2O_3–NF SC

enhancement originates from the cooperative action of the conductive carbon coating and the electroactive ZnO–Al_2O_3 scaffold, which jointly facilitate electron transport, promote redox reactions, and ensure rapid accessibility of ions. As the scan rate increased, anodic peaks shifted slightly toward more positive potentials while cathodic peaks moved toward more negative values, reflecting the quasi-reversible nature of the underlying redox processes. The preservation of well-defined peak shapes over the entire scan rate range further indicates stable charge transfer kinetics, efficient ionic diffusion, and low resistive losses within the hybrid network. Such behavior emphasizes that the conductive carbon layer not only improves electronic pathways but also stabilizes the electrode/electrolyte interface, thereby mitigating polarization effects during fast charge–discharge operations. These observations strongly suggest that ZnO-NR@C/Al_2O_3–NF is capable of delivering reliable and high rate performance, consistent with recent reports on hybrid metal oxide/carbon pseudocapacitive systems that display excellent redox reversibility and conductivity-enhanced energy storage behavior [40, 41].

A comprehensive kinetic investigation was carried out on SCs assembled with ZnO–NR/Al_2O_3–NF and ZnO–NR@C/Al_2O_3–NF electrodes in order to clarify the underlying charge storage mechanism. The dependence of peak current on scan rate followed the power-law relation $i = av^b$, where the exponent b indicates whether the process is diffusion-controlled or surface-confined. A value near 0.5 typically reflects ion diffusion–dominated faradaic behavior, whereas a value approaching unity corresponds to capacitive contributions [42, 43]. Analysis of the log(i)–log(ν) plots yielded b-values of 0.66 for ZnO–NR/Al_2O_3–NF-based devices and 0.71 for ZnO-NR@C/Al_2O_3–NF-based devices. The higher b-value in the latter confirms that the incorporation of carbon enhances capacitive participation by promoting faster charge transfer and improved access to electroactive sites.

To further differentiate between capacitive and diffusion-governed contributions, the current at each potential was separated using the relation

$i(V) = k_1\nu + k_2\nu^{1/2}$, where k_1 and k_2 denote the capacitive and diffusion-controlled components, respectively. The transformed equation $i/\nu^{1/2} = k_1\nu^{1/2} + k_2$ allowed quantitative evaluation of these contributions [44–46]. As shown in Fig. 3c, d, the capacitive fraction increased steadily with scan rate for both systems, indicating that surface-driven reactions become progressively dominant at higher sweep speeds. At 100 mV s^{-1}, the capacitive share reached 45% for the ZnO-NR/Al_2O_3–NF SC and 59% for the ZnO-NR@C/Al_2O_3–NF device (Fig. 3e–f). This enhancement demonstrates the effective role of the conductive carbon layer, which not only accelerates electron mobility but also improves ion transport pathways within the electrode–electrolyte interface.

Overall, the results confirm that ZnO–NR@C/Al_2O_3–NF-based SCs operate predominantly through pseudocapacitive mechanisms involving fast and reversible surface-confined redox reactions rather than sluggish intercalation processes. The ability to sustain a high capacitive contribution even at moderate scan rates highlights the advantages of the hierarchical composite structure in minimizing charge transfer resistance and facilitating rapid ion diffusion. These features, mechanical integrity from the Al_2O_3 scaffold combined with enhanced conductivity and stability from the carbon coating, collectively underpin the excellent reversibility, rate performance, and long-term durability of the system, validating ZnO-NR@C/Al_2O_3–NF as a highly promising design for next-generation high power energy storage.

To further assess the charge storage behavior of the assembled SCs, galvanostatic charge–discharge (GCD) experiments were conducted for devices employing ZnO–NR@C/Al_2O_3–NF and ZnO-NR–Al_2O_3–NF electrodes at current densities between 1 and 4 A g^{-1}, as illustrated in Fig. 4a, b. The obtained GCD traces exhibit clear deviations from linearity, a hallmark of pseudocapacitive systems in which energy storage originates mainly from quasi-reversible redox reactions occurring at or near the electrode surface rather than simple electrostatic accumulation. Among the two systems, the ZnO-NR@C/Al_2O_3–NF SC consistently displayed longer discharge times under identical

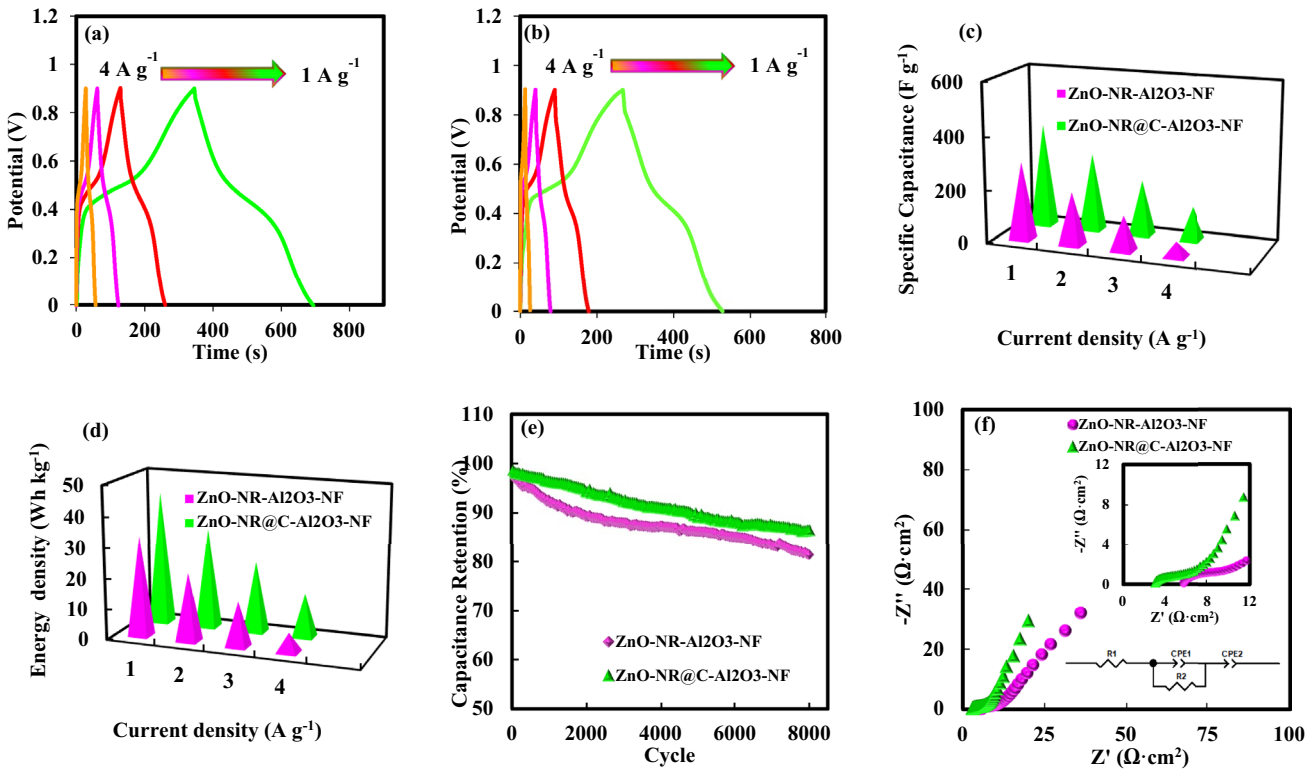

Fig. 4 **a**, **b** GCD curves of SCs assembled with ZnO-NR@C/Al_2O_3–NF and ZnO-NR/Al_2O_3–NF electrodes at different current densities. **c** Comparison of specific capacitance versus current density. **d** Energy density as a function of current density for both systems. **e** Capacitance retention measured at 4 A g^{-1}. **f** Nyquist impedance spectra of the two devices, with the fitted equivalent circuit shown in the inset

conditions, evidencing superior electron transport, more efficient ion diffusion pathways, and improved reversibility of redox processes. Additionally, the consistent shape of the charge–discharge curves across different current densities highlights the stability of the capacitive response over a wide operational window.

The quantitative evaluation of electrochemical performance parameters was carried out using the GCD data. The specific capacitance (C_sp, F g^{-1}) was calculated from the relation Csp = (I × Δt) / (m × ΔV), where I is the applied current, Δt is the discharge time, m is the mass of active material, and ΔV is the potential window. From these values, the energy density (E, Wh kg^{-1}) was further estimated using the expression E = ½ × Csp × $(\Delta V)^2$/ 3.6 [46, 47]. The derived values are summarized in Fig. 4c, d, confirming that the incorporation of the conductive carbon layer into the ZnO–Al_2O_3 scaffold results in markedly improved charge storage capability and energy delivery. As shown in Fig. 4a, b, the GCD curves of the SCs assembled with ZnO–NR@C/Al_2O_3–NF and ZnO-NR–Al_2O_3–NF electrodes exhibit quasi-capacitive characteristics, consistent with pseudocapacitive behavior identified in the CV tests. Among the two, the ZnO–NR@C/Al_2O_3–NF device delivers the longest discharge duration at comparable current densities, clearly demonstrating superior charge storage capability. At 1 A g^{-1}, this system achieved a specific capacitance of 388.33 F g^{-1} with an energy density of 43.68 Wh kg^{-1}, significantly surpassing the ZnO-NR/Al_2O_3–NF counterpart, as illustrated in Fig. 4c, d. The remarkable enhancement in performance arises from the synergistic role of the carbon coating and the ZnO–Al_2O_3 framework, which together provide a larger electroactive surface, faster charge transfer kinetics, and more efficient ion transport pathways.

These results confirm that the hierarchical composite design effectively minimizes resistive losses, facilitates reversible faradaic reactions, and maintains structural integrity during cycling. The combined contribution of the robust Al_2O_3 nanofiber scaffold and the conductive carbon layer ensures long-term durability, high rate performance, and reliable energy delivery, positioning the ZnO-NR@C–Al_2O_3–NF-based SC as a strong candidate for advanced high power energy storage applications.

Long-term durability of the SCs was further examined by subjecting the devices to 8000 consecutive charge–discharge cycles at a relatively high current density of 4 A g^{-1} (Fig. 4e). Even after prolonged cycling, both systems preserved most of their initial capacitance, with retention values of 86.38% for the ZnO-NR@C/Al_2O_3–NF-based device and 81.32% for the ZnO-NR/Al_2O_3–NF counterpart. These results clearly demonstrate that the fabricated SCs exhibit highly stable electrochemical performance and robust charge–discharge behavior, while the ZnO-NR@C/Al_2O_3–NF configuration maintains a distinct advantage in terms of capacitance retention, underscoring its superior cycling stability and reliability for long-term energy storage applications.

Electrochemical impedance spectroscopy (EIS) was employed to further elucidate the charge transport properties and interfacial kinetics of SCs based on ZnO-NR/Al_2O_3–NF and ZnO-NR@C/Al_2O_3–NF electrodes. The Nyquist spectra, shown in Fig. 4f, were recorded over a wide frequency range of 0.01 Hz to 100 kHz and interpreted using an equivalent circuit model. This model consists of essential elements, including the equivalent series resistance (R_{ESR}), charge transfer resistance (R_{ct}), and two constant phase elements (CPE-1 and CPE-2), which account for the double-layer capacitance and the pseudocapacitive contribution, respectively [45, 48, 49]. In the high-frequency domain, the semicircle diameter reflects the magnitude of R_{ct}, thereby describing the efficiency of electron exchange processes occurring at the electrode–electrolyte interface. By contrast, the inclined line observed in the low-frequency region corresponds to Warburg-type diffusion behavior, which reveals the influence of ionic transport limitations inside the porous electrode matrix. Furthermore, the intercept of the semicircle with the real axis at high frequencies indicates the R_{ESR}, encompassing the intrinsic resistance of the electrode material, the ionic resistance of the electrolyte, contributions from the current collector, and contact resistances at the interface. Impedance measurements further distinguish the electrical characteristics of the fabricated SCs. The ZnO-NR/Al_2O_3–NF device exhibited the highest R_{ESR} of 5.73 Ω, while the ZnO-NR@C/Al_2O_3–NF system showed a markedly lower value of 3.04 Ω. A similar trend was observed for the R_{ct}, where the composite-based SC registered only 3.26 Ω compared with 6.63 Ω for its uncoated counterpart. The notable reduction in both R_{ESR} and R_{ct} for the ZnO-NR@C/Al_2O_3–NF configuration confirms its superior ability to facilitate ion migration and accelerate electron exchange at the electrode–electrolyte interface.

These improvements arise from the conductive carbon shell, which establishes continuous electron pathways, and the porous ZnO–Al_2O_3 scaffold, which provides accessible active sites for redox reactions. The combination of low internal resistance, efficient charge transport, and robust structural support results in stable and rapid electrochemical kinetics. Collectively, these features explain the enhanced cycling stability and high rate capability of the composite system, underscoring its promise as a durable and high-performance platform for next-generation SC applications.

4 Conclusion

In summary, we have successfully designed and synthesized a novel binder-free hierarchical composite, ZnO–NR@C/Al_2O_3–NF, tailored for supercapacitor applications. The material was fabricated through a multi-step process involving electrospinning, hydrothermal growth, and carbonization. Comprehensive structural and compositional analyses confirmed its distinctive architecture and high purity. The exceptional electrochemical performance arises from the synergistic interplay between its components: the robust Al_2O_3 scaffold ensures mechanical stability, the ZnO nanorods provide abundant active sites, and the conformal carbon coating enhances electrical conductivity while serving as a protective buffer layer. This intelligently designed architecture delivered a high specific capacitance of 388.33 F g^{-1} and a corresponding energy density of 43.68 Wh kg^{-1} at a current density of 1 A g^{-1}. Furthermore, the composite demonstrated remarkable long-term durability, maintaining 86.38% of its initial capacitance after 8000 charge–discharge cycles. This combination of high performance and structural resilience validates our rational and scalable strategy for engineering durable, high-performance materials for next-generation energy storage systems.

Author Contributions

All authors contributed equally to this work with the following shared roles: validation, formal analysis, writing—review & editing, investigation, funding acquisition for the research, and software. Additionally, H. A El Sabban took on project administration responsibilities.

Funding

The authors extend their appreciation to the Deanship of Research and Graduate Studies at King Khalid University for funding this work through Large Research Project under grant number RGP2/448/46.

Data availability

They are available from the corresponding author upon reasonable request.

Declarations

Conflict of interests The authors declare that they have no known competing financial interests or personal relationships that could have appeared to influence the work reported in this paper.

Ethical approval This research did not involve human participants, animal subjects, or any procedures requiring ethical approval from an institutional review board (IRB) or animal ethics committee.

References

1. C.-Y. Hsu, A. Basem, P.K. Singh, A.M.A. Mohamed, M. Latipova, S. Usanov, R. Siddikov, M. Diab, I. Mahariq, A.S. Shaik, S. Islam, Harnessing boron nitride monolayers with dodecagonal porous as an anode material in potassium ion batteries: A computational study. J. Electroanal. Chem. **1002**, 119728 (2026)
2. R. Khan, I. Omar, A.A. Alizadeh, N.S.S. Singh, M.A. Hussein, A.M. Sadeq, H. Rajab, K. Hajlaoui, AI-enhanced design of liquid-PCM hybrid cooling for li-ion batteries: GA-MLPNN modeling integrated with multi-objective artificial vultures optimization. J. Energy Storage **144**, 119701 (2026)
3. M.H. Abdulameer, A.T. Ahmed, I. Mahariq, P. Kanjariya, A. Rajiv, A. Shankhyan, S. Jaidka, M.A. Rusho, H. Kumar, M. Ahmed, H.M. Alkahtani, Potential application of BC2N nanotube semiconductors in the Li-ion batteries. Mater. Chem. Phys. **343**, 131057 (2025)

4. Y. Jia, Y. Ma, Advances in MoO_3-based supercapacitors for electrochemical energy storage. J. Energy Storage **85**, 111103 (2024)
5. I. Marouani, A.B.M. Ali, Z. Algarni, S.A. Aldaghfag, D. Jumanazarov, A. Amari, B. Madaminov, O. Mukhitdinov, I. Mahariq, Construction of a novel Fe_2O_3-loaded g-C_3N_4 electrodes for high-energy and sustainable asymmetric hybrid supercapacitors. Surf. Interfaces **73**, 107481 (2025)
6. R. Nair, K. Uppuluri, F. Paul, K. Sirengo, D. Szwagierczak, S.C. Pillai, L. Manjakkal, Electrochemical energy storing performances of printed LaFeO3 coated with PEDOT: PSS for hybrid supercapacitors. Chem. Eng. J. **504**, 158781 (2025)
7. M. Vijayalakshmi, R. Wang, W.Y. Jang, R.R. Kakarla, C.V. Reddy, F. Alonso-Marroquin, P. Anjana, B. Cheolho, J. Shim, T.M. Aminabhavi, Ternary g-C3N4/Co3O4/CeO2 nanostructured composites for electrochemical energy storage supercapacitors. J. Environ. Manage. **370**, 122996 (2024)
8. C. Wang, J. Hao, L. Duan, D. Zhao, Y. Ma, J. Zhang, P. Ma, D. Han, F. Meng, Energy storage performance with ultrahigh energy density and power density of Ba0. 85Ca0. 15Zr0. 1Ti0. 9O3-based lead-free ceramics through synergistic optimization. Ceram. Int. **51**, 35133–35143 (2025)
9. C.V.M. Gopi, S. Alzahmi, V. Narayanaswamy, R. Vinodh, B. Issa, I.M. Obaidat, Supercapacitors: a promising solution for sustainable energy storage and diverse applications. J. Energy Storage **114**, 115729 (2025)
10. J. Yan, Q. Wang, T. Wei, Z. Fan, Recent advances in design and fabrication of electrochemical supercapacitors with high energy densities. Adv. Energy Mater. **4**, 1300816 (2014)
11. C. Choi, D.S. Ashby, D.M. Butts, R.H. DeBlock, Q. Wei, J. Lau, B. Dunn, Achieving high energy density and high power density with pseudocapacitive materials. Nat. Rev. Mater. **5**, 5–19 (2020)
12. J. Libich, J. Máca, J. Vondrák, O. Čech, M. Sedlaříková, Supercapacitors: properties and applications. J. Energy Storage **17**, 224–227 (2018)
13. X. Chen, R. Paul, L. Dai, Carbon-based supercapacitors for efficient energy storage. Natl. Sci. Rev. **4**, 453–489 (2017)
14. K. Sheoran, V.K. Thakur, S.S. Siwal, Synthesis and overview of carbon-based materials for high performance energy storage application: a review. Mater. Today Proc. **56**, 9–17 (2022)
15. T. Wang, X. Zang, X. Wang, X. Gu, Q. Shao, N. Cao, Recent advances in fluorine-doped/fluorinated carbon-based materials for supercapacitors. Energy Storage Mater. **30**, 367–384 (2020)
16. R.R. Salunkhe, Y.V. Kaneti, Y. Yamauchi, Metal–organic framework-derived nanoporous metal oxides toward supercapacitor applications: progress and prospects. ACS Nano **11**, 5293–5308 (2017)
17. H. Qi, C. He, C. Song, J. Gao, Q. Gao, W. Luo, Z. Zhang, H. Liu, X. Yuan, W. Wu, Tailoring the exposure of active facets of FeNCN toward enhanced pseudocapacitive behavior for sodium storage. Chin. Chem. Lett. (2025). https://doi.org/10.1016/j.cclet.2025.111591
18. Y. Chen, F. Xu, L. Sun, Y. Zhu, Y. Feng, R. Xu, C. Yu, X. Hu, M. Du, R. Li, *Ganoderma lucidum*-derived porous carbon loaded nano-flower balls metal oxides for energy storage application in supercapacitors. J. Energy Storage **130**, 117329 (2025)
19. A. Surulinathan, H. Gubendran, B. Sambandam, S. Ganapathy, A. Ayyaswamy, Mixed metal oxide-based binder-free electrode and redox additive electrolyte combination for enhanced supercapacitor performance. J. Alloys Compd. **988**, 174164 (2024)
20. A. Sanni, D. Govindarajan, S. Nijpanich, W. Limphirat, A.A. Mohamad, J. Theerthagiri, M.Y. Choi, S. Kheawhom, Unveiling a paradigm shift in supercapacitor dynamics: γ-Al2O3-infused ZnO nanorods with redox-active K4Fe (CN) 6 alkaline electrolytes. J. Alloys Compd. **1010**, 177892 (2025)
21 D.U. Asangi, B.S. Chikkatti, A.M. Sajjan, N.R. Banapurmath, T.Y. Khan, S.W. Ghori, S.A. Huddar, S. Rajappa, Electrochemical investigation of Al2O3-CuO binary nanocomposite electrodes: Towards high energy storage supercapacitors. J. Alloys Compd. (2025). https://doi.org/10.1016/j.jallcom.2025.180806
22. H. Gao, X. Cheng, B. Joshi, E. Samuel, J. Zhang, A. Aldalbahi, G. Periyasami, Q. Wei, S.S. Yoon, Augmenting energy storage capacity of aqueous-electrolyte-based supercapacitors: integrating multivalent vanadium into freestanding ZnO/carbon nanofiber electrodes. J. Energy Storage **99**, 113204 (2024)
23. A.B.M. Ali, A.A. Mohammed, N.S.S. Singh, M.A. Rusho, A. Abilkasimov, B. Saydullaev, L. Safarova, A. Smerat, A.I. Ali, S. Islam, M.I. Khan, Green synthesized Zinc oxide nanoparticles mediated by Thymus pannonicus extract as a novel catalyst in the reduction of aromatic nitro compounds. J. Organomet. Chem. **1040**, 123817 (2025)
24. K. Santhy, S. Thorat, P. Pukale, M. Salot, G. Avasthi, D. Mandal, A. Pramanick, S. Singh, S. Chaudhury, A new eco-friendly process for the synthesis of Al-doped ZnO nanopowder: structure and supercapacitance characteristics. Ceram. Int. (2025). https://doi.org/10.1016/j.ceramint.2025.06.295

25. M. Saranya, R. Ramachandran, F. Wang, Graphene-zinc oxide (G-ZnO) nanocomposite for electrochemical supercapacitor applications. J. Sci. Adv. Mater. Devices **1**, 454–460 (2016)
26. S. Pandiyarajan, S.S.M. Manickaraj, A.-H. Liao, A.R.P. Selvam, K.-Y. Lee, H.-C. Chuang, Coherent construction of recovered γ-Al2O3 embedded N-doped activated carbon by supercritical-CO2 pathway: robust hybrid electrode material for energy storage device. J. Alloys Compd. **936**, 168213 (2023)
27. Y. Guo, N. Sheng, C. Zhu, Preparation of Al@ Al2O3 macrocapsules with high durability for high-temperature thermal storage. ACS Sustainable Chem. Eng. **10**, 6426–6433 (2022)
28. M.A. Ebied, M.A. Azim, A. Emad-Eldeen, AI-based approach for predicting the storage performance of zinc oxide-based supercapacitor electrodes. J. Energy Storage **94**, 112292 (2024)
29. M.F. Iqbal, M.N. Ashiq, S. Iqbal, N. Bibi, B. Parveen, High specific capacitance and energy density of synthesized graphene oxide based hierarchical Al2S3 nanorambutan for supercapacitor applications. Electrochim. Acta **246**, 1097–1103 (2017)
30. S. Rajan, A. Venugopal, H. Kozhikkalathil, S. Valappil, M. Kale, M. Mann, P. Ahuja, S. Munjal, (2023) Synthesis of ZnO nanoparticles by precipitation method Characterizations and applications in decipherment of latent fingerprints, Materials Today Proceedings.
31. A. Goktas, S. Modanlı, A. Tumbul, A. Kilic, Facile synthesis and characterization of ZnO, ZnO: Co, and ZnO/ZnO: Co nano rod-like homojunction thin films: role of crystallite/grain size and microstrain in photocatalytic performance. J. Alloys Compd. **893**, 162334 (2022)
32. C. Cheng, H. Liu, C. Ouyang, N. Hu, G. Zha, H. Hou, A high-temperature stable composite polyurethane separator coated Al2O3 particles for lithium ion battery. Compos. Commun. **33**, 101217 (2022)
33. M. Qian, T. Xue, S. Fan, L. Zhang, Q. Zhou, Y. Xu, X. Wang, J. Tang, S. Chen, L. Hu, Influence of ZrO2 content on the chemical durability and structure of P2O5-Fe2O3-Al2O3-Na2O-ZrO2 glass ceramics. J. Non-Cryst. Solids **582**, 121446 (2022)
34. M. Chen, F.-M. Liu, S.-S. Chen, Y.-J. Zhao, Y. Sun, C.-S. Li, Z.-Y. Yuan, X. Qian, R. Wan, In situ self-catalyzed formation of carbon nanotube wrapped and amorphous nanocarbon shell coated LiFePO4 microclew for high-power lithium ion batteries. Carbon **203**, 661–670 (2023)
35. J. Hu, Y. Li, Y. Zhen, M. Chen, H. Wan, In situ FTIR and ex situ XPS/HS-LEIS study of supported Cu/Al2O3 and Cu/ZnO catalysts for CO2 hydrogenation. Chin. J. Catal. **42**, 367–375 (2021)
36. X. Lin, Z. Wang, X. Jiang, T. Ning, Y. Jiang, A. Lu, Effect of Al2O3/SiO2 mass ratio on the structure and properties of medical neutral boroaluminosilicate glass based on XPS and infrared analysis. Ceram. Int. **49**, 38499–38508 (2023)
37. M. Ismail, C. Mahata, S. Kim, Forming-free Pt/Al2O3/HfO2/HfAlOx/TiN memristor with controllable multilevel resistive switching and neuromorphic characteristics for artificial synapse. J. Alloys Compd. **892**, 162141 (2022)
38. J. Wu, P. Zhang, D. Xu, X. Chen, Y. Wang, Y. Fan, S. Yu, M. Wu, Effect of carbonization temperature on electrochemical properties of ZnO@ C anode materials. J. Electroanal. Chem. **909**, 116121 (2022)
39. M. Zhang, W. Zhou, H. Xu, Electrostatic self-assembly design of core@ shell structured Al2O3@ C nanospheres towards high-efficiency and damage-free polishing sapphire wafer. J. Alloys Compd. **859**, 158248 (2021)
40. D. Yang, M.I. Ionescu, (2017) Metal oxide–carbon hybrid materials for application in supercapacitors, in: Metal Oxides in supercapacitors, Elsevier, 193–218.
41. D. Govindarajan, A. Sanni, W. Limphirat, K. Kirubaharan, G. Murugadoss, A.A. Mohamad, T. Yonezawa, S. Kheawhom, Atomic-level synergy in multi-valent metal oxide-graphene composites for ultra-high-performance supercapacitors. J. Alloys Compd. **1039**, 183022 (2025)
42. S.M.H. Jafari-Mousavi, F.A. Peyghan, M. Mirzaei-Saatlo, E. Asghari, Electrodeposition of poly (aniline-co-4-nitroaniline)/CoAl-layered double hydroxide composites as electrode materials for supercapacitor applications. Inorg. Chem. Commun. **177**, 114450 (2025)
43. J. Liu, J. Wang, C. Xu, H. Jiang, C. Li, L. Zhang, J. Lin, Z.X. Shen, Advanced energy storage devices: basic principles, analytical methods, and rational materials design. Adv. Sci. **5**, 1700322 (2018)
44. M. Zhang, J. Zhou, J. Yu, L. Shi, M. Ji, H. Liu, D. Li, C. Zhu, J. Xu, Mixed analogous heterostructure based on MXene and prussian blue analog derivative for high-performance flexible energy storage. Chem. Eng. J. **387**, 123170 (2020)
45. V. Augustyn, P. Simon, B. Dunn, Pseudocapacitive oxide materials for high-rate electrochemical energy storage. Energy Environ. Sci. **7**, 1597–1614 (2014)
46. V. Nithya, A review on holey graphene electrode for supercapacitor. J. Energy Storage **44**, 103380 (2021)
47. M. Safari-Gezaz, M. Mirzaei-Saatlo, E. Asghari, M. Parhizkar, The incorporation of cobalt ions into hydroxyapatite nanostructure for a novel range of electrochemical energy storage applications. J. Phys. Chem. Solids **192**, 112118 (2024)

48. M. Mirzaei-Saatlo, E. Asghari, H. Shekaari, B. Pollet, R. Vinodh, Performance of ethanolamine-based ionic liquids as novel green electrolytes for the electrochemical energy storage applications. Electrochim. Acta **474**, 143499 (2024)
49. A.E. Reddy, T. Anitha, C.V.M. Gopi, I.K. Durga, H.-J. Kim, Facile synthesis of hierarchical ZnMn 2 O 4@ ZnFe 2 O 4 microspheres on nickel foam for high-performance supercapacitor applications. New J. Chem. **42**, 2964–2969 (2018)